ATLAS CONF Note

ATLAS-CONF-2023-038

19th July 2023

Evidence of pair-production of longitudinally polarised vector bosons and study of CP properties in $ZZ \to 4\ell$ events with the ATLAS detector at $\sqrt{s} = 13$ TeV

The ATLAS Collaboration

A study of the polarisation and CP properties in ZZ production is presented. The used data set corresponds to an integrated luminosity of 140 fb^{-1} of proton–proton collisions at a centre-of-mass energy of 13 TeV recorded by the ATLAS detector at the Large Hadron Collider. The ZZ candidate events are reconstructed using two same-flavour opposite-charge electron or muon pairs. The production of two longitudinally polarised Z bosons is measured with a significance of 4.3 standard deviations, and its cross-section is measured in a fiducial phase space to be 2.44 ± 0.59 fb, consistent with the next-to-leading order Standard Model prediction of 2.09 ± 0.10 fb. Differential cross-section of the inclusive ZZ production as a function of a CP-sensitive angular observable is also measured. The results are used to constrain anomalous CP-odd neutral triple gauge couplings.

ATLAS-CONF-2023-038
19 July 2023

1 Introduction

Measurements of Z boson pair (ZZ) production in proton–proton (pp) collisions at the Large Hadron Collider (LHC) provide an important test of the Standard Model (SM) gauge structure in the electroweak (EW) sector. Representative leading-order Feynman diagrams of ZZ production at the LHC are shown in Figure 1. With increased luminosity, experimental data enables property studies beyond precision measurements of integrated and differential cross-sections, such as the weak boson polarisation and charge (C) and parity (P) properties. The polarisation measurement of massive weak bosons is a direct probe of the Electroweak Symmetry Breaking mechanism, through which the W and Z bosons obtain the longitudinally polarised state. Diboson polarisation measurements and especially those probing longitudinally polarised vector bosons provides unique sensitivity to new physics beyond the SM (BSM) [1].

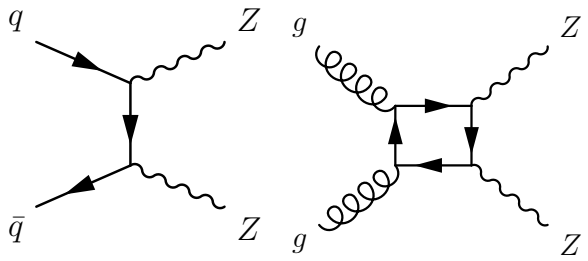

Figure 1: Examples of main leading-order Feynman diagrams for ZZ production in pp collisions: (a) $q\bar{q}$-initiated, (b) gg-initiated.

Polarisation measurements performed with LHC data have been mainly focused on single bosons such as in W boson production [2, 3], Z boson production [4, 5] and $t\bar{t}$ production [6–8]. Single-boson polarisation states have also been measured in WZ production by the ATLAS [9] and CMS [10] Collaborations. Recently first measurements on joint-polarisation states of weak bosons have also been reported, using EW production of same-sign $W^{\pm}W^{\pm}$ boson pairs by the CMS Collaboration [11] and inclusive WZ production by the ATLAS Collaboration [12]. In the latter, the fraction of diboson events with a simultaneous longitudinal polarisation (LL) is observed with a significance of 7.1 standard deviations.

This paper presents a measurement of the production of two longitudinally polarised Z bosons ($Z_{\mathrm{L}}Z_{\mathrm{L}}$) in the decay channel $ZZ \to \ell^+\ell^-\ell'^+\ell'^-$, where ℓ and ℓ' can be an electron or a muon. The Z boson candidates are reconstructed with same-flavour, opposite-charge (SFOC) electron or muon pairs, and they are required to be on-shell with $|m_{\ell\ell} - m_Z| < 10$ GeV, where $m_{\ell\ell}$ is the invariant mass of the lepton pair and m_Z is the Z boson pole mass [13].

The violation of CP symmetries is required to explain the matter-antimatter asymmetry in the Universe, and it is well known that there is insufficient CP violation in the SM [14–16]. The measurement of CP-sensitive observables in diboson production can be utilised to explore new sources of CP violation in the gauge-boson sector. CP-violating effects in weak-boson self-interactions have been probed in various measurements of diboson production at the LHC by constraining the CP-odd anomalous neutral triple gauge coupling (aNTGC), including ZZZ and $ZZ\gamma$ vertexes, using ZZ production in ATLAS and CMS [17–23]. Such experimental searches are mainly performed in the form of extracting anomalous triple gauge boson couplings (aTGC) using event rates or cross-section measurements without using dedicated CP-sensitive observables.

This paper presents the differential cross-section for a dedicated CP-odd angular observable, referred to as the *Optimal Observable* (OO), defined using the decay products of weak bosons in ZZ production, which has the advantage of being sensitive to BSM amplitudes through the interference to the SM [24, 25]. The results are then reinterpreted to constrain aNTGC using an effective vertex function approach [26]. The ATLAS Collaboration has previously used such type of dedicated CP-sensitive observables in the EW Zjj production to test CP violation in the weak-boson self-interactions [27].

The CP property is studied using an aNTGC vertex that can be parameterised with two coupling parameters f_Z^4 and f_γ^4 that violate CP symmetry. In the presence of such parameters, the cross-section in any given bin of the CP-sensitive observable can be parameterised as

$$\sigma^i = \sigma^i_{\text{SM}} + c \cdot \sigma^i_{\text{interference}} + c^2 \cdot \sigma^i_{\text{quadratic}}, \tag{1}$$

where the superscript i is the bin index of the CP-sensitive observable, c is the CP-odd aNTGC, σ^i_{SM} is the prediction from the SM, $\sigma^i_{\text{interference}}$ is the linear interference between SM and the aNTGC, and $\sigma^i_{\text{quadratic}}$ is the quadratic contribution of the aNTGC. As pointed out in Ref. [28], for aNTGC, the quadratic term dominates over the linear interference term. Existing constraints on CP-odd aNTGC stem primarily from their effect on the cross-section in the high-p_{T} regime, using kinematic observables such as the leading p_{T}^Z. Such high-p_{T} sensitive kinematic observables cannot distinguish CP-even and CP-odd effects. This paper presents a search for CP violation using the unfolded OO which is sensitive to the interference terms.

2 ATLAS detector

The ATLAS experiment [29] at the LHC is a multipurpose particle detector with a forward–backward symmetric cylindrical geometry and a near 4π coverage in solid angle.[1] It consists of an inner tracking detector (ID) surrounded by a thin superconducting solenoid providing a 2 T axial magnetic field, electromagnetic and hadron calorimeters, and a muon spectrometer (MS). The inner tracking detector covers the pseudorapidity range $|\eta| < 2.5$. It consists of silicon pixel, silicon microstrip, and transition radiation tracking detectors. Lead/liquid-argon (LAr) sampling calorimeters provide electromagnetic (EM) energy measurements with high granularity. A steel/scintillator-tile hadron calorimeter covers the central pseudorapidity range ($|\eta| < 1.7$). The endcap and forward regions are instrumented with LAr calorimeters for both the EM and hadronic energy measurements up to $|\eta| = 4.9$. The muon spectrometer surrounds the calorimeters and is based on three large superconducting air-core toroidal magnets with eight coils each. The field integral of the toroids ranges between 2.0 and 6.0 T m across most of the detector. The muon spectrometer includes a system of precision tracking chambers and fast detectors for triggering. A two-level trigger system is used to select events. The first-level trigger is implemented in hardware and uses a subset of the detector information to accept events at a rate below 100 kHz. This is followed by a software-based trigger that reduces the accepted event rate to 1 kHz on average depending on the data-taking conditions. An extensive software suite [30] is used in data simulation, in the reconstruction and analysis of real and simulated data, in detector operations, and in the trigger and data acquisition systems of the experiment.

[1] ATLAS uses a right-handed coordinate system with its origin at the nominal interaction point (IP) in the centre of the detector and the z-axis along the beam pipe. The x-axis points from the IP to the centre of the LHC ring, and the y-axis points upwards. Cylindrical coordinates (r, ϕ) are used in the transverse plane, ϕ being the azimuthal angle around the z-axis. The pseudorapidity is defined in terms of the polar angle θ as $\eta = -\ln\tan(\theta/2)$. Angular distance is measured in units of $\Delta R \equiv \sqrt{(\Delta\eta)^2 + (\Delta\phi)^2}$.

3 Data and simulation

The data collected by the ATLAS experiment during the 2015-2018 data-taking period of the LHC at a centre-of-mass energy of $\sqrt{s}$ = 13 TeV is analysed, and corresponds to an integrated luminosity of 140 fb^{-1}. The data events are triggered using single-lepton and dilepton triggers with the minimum trigger threshold, depending on data-taking periods, varying between 20 – 26 GeV for single-lepton triggers and 8 – 24 GeV for dilepton triggers [31, 32]. The trigger efficiency is nearly 100% for signal events after offline event selections.

Simulations of the signal SM processes of the on-shell production of two Z bosons and background processes resulting in two SFOC lepton pairs are derived using the Monte Carlo (MC) generators. The parton-initiated $q\bar{q} \to ZZ$ (Figure 1(a)) process was modelled using the Sherpa 2.2.2 generator [33]. The matrix elements (ME) were calculated with next-to-leading order (NLO) accuracy in QCD for up to one additional parton emission and leading-order (LO) accuracy for up to three additional parton emissions. The matrix element calculations were matched and merged with the Sherpa parton shower based on Catani-Seymour dipole factorisation [34, 35], using the MEPS@NLO prescription [36–38]. The virtual QCD corrections were provided by the OpenLoops library [39–41]. The NNPDF3.0nnlo set of parton distribution function (PDF) [42] and the dedicated set of tuned parton-shower parameters developed by the Sherpa authors were used for generating this sample. The higher-order corrections from NLO electroweak effects were taken into account for the $q\bar{q} \to ZZ$ sample by applying reweighting corrections as a function of $m_{4\ell}$ [43, 44].

An alternative prediction of the $q\bar{q} \to ZZ$ process with Powheg−Box v2 [45–47] is used for estimating the theory modeling uncertainty. This sample was generated at NLO accuracy in QCD and interfaced with Pythia 8.186 [48] for modelling the parton shower, hadronisation, and effect of underlying events with parameters set according to the AZNLO tune [49]. For the hard-scattering and parton showering, CT10 PDF [50] and CTEQ6L1 PDF [51] sets were used, respectively. A higher-order correction as a function of $m_{4\ell}$ was obtained using a Matrix NNLO QCD prediction [52–55] and applied to these events. The correction was defined as the ratio of the cross-section at NNLO QCD accuracy to the one at NLO QCD accuracy.

The loop-induced $gg \to ZZ$ process (Figure 1(b)) was also modelled with the Sherpa 2.2.2 generator using ME calculated with LO accuracy for up to one additional parton emission. As detailed in Ref. [56], the higher-order QCD effects are accounted for by normalising the LO prediction to NLO [57, 58] and NNLO [59, 60] predictions. The same parton showering, matching, and merging schemes as for the Sherpa $q\bar{q} \to ZZ$ simulations were used. The EW production of ZZ in association with two jets, $qq \to ZZjj$, was modelled by MadGraph5_aMC@NLO 2.6.7 [61]. The matrix element was calculated at LO in QCD, and the NNPDF3.0nnlo PDF set was used. Pythia 8.244 [62] tuned with the $A14$ tune parameters [63] was used to simulate parton showering, hadronisation, and underlying-event activity for the electroweak $qq \to ZZjj$ events. The three processes, parton-initiated $q\bar{q} \to ZZ$, loop-induced $gg \to ZZ$, and electroweak $qq \to ZZjj$, collectively simulate the total signal events for this measurement.

In addition to the simulations for the inclusive ZZ production, samples for different polarisation states were also produced. The polarised $q\bar{q} \to ZZ$ signal samples were generated using MadGraph5_aMC@NLO 2.7.3 [61, 64], with ME calculated at LO in perturbative QCD and with the NNPDF3.0nlo [42] PDF set. The events were interfaced to Pythia 8.240 to model the parton shower, hadronisation, and underlying event, with parameters set according to the A14 tune and using the NNPDF2.3lo [65] set of PDFs. Polarised samples were simulated corresponding to the three helicity

states, Z_TZ_T for two transversely polarised Z bosons, Z_TZ_L for one transversely polarised Z boson and one longitudinally polarised Z boson, and Z_LZ_L for two longitudinally polarised Z bosons, respectively, with each Z boson decaying independently into an electron or a muon pair. The Z boson polarisation is defined in the centre-of-mass (CM) frame of the two Z bosons, which is a natural choice for diboson production [66]. To account for the real part of the NLO corrections, the QCD-induced events were simulated with up to two jets in the matrix element at LO and merged with PYTHIA 8 parton showers using the CKKW-L scheme [67, 68]. The EW production of the polarised ZZ samples was generated with MADGRAPH5_AMC@NLO 2.7.3 similarly, and they are used together with the QCD-induced $q\bar{q} \to ZZ$ samples in the analysis. The generation of polarised MC events for the loop-induced $gg \to ZZ$ process is not possible.

Background events consist of four-lepton events originating from $t\bar{t}Z$ and VVZ processes, as well as four-lepton events containing at least one non-prompt lepton. The $t\bar{t}Z$ events were modelled by SHERPA 2.2.0 generator at LO accuracy with up to one additional parton emission using the MEPS@LO setup [37, 38] and the NNPDF3.0NNLO PDF set. The sample was scaled to reproduce the prior $t\bar{t}Z$ cross-section measurement from ATLAS [69]. Events from the VVZ processes were simulated by the Sherpa 2.2.2 generator with NLO accuracy in QCD for the inclusive process and LO accuracy in QCD for up to two additional parton emissions. The NNPDF3.0NNLO PDF set and the default SHERPA parton showering scheme were used. The prediction was scaled to match the prior measurement of the triboson production from ATLAS [70].

The events with either of the four leptons originating from non-prompt sources are estimated using a semi-data-driven method discussed in Section 5. The method uses information about the origin of the non-prompt leptons from simulations of the relevant processes. The production of WZ with the leptonic decays of vector bosons was modelled with SHERPA 2.2.2. The same setup and parameters as for the $q\bar{q} \to ZZ$ modelling were used. The events with non-prompt leptons arising from Z + jets processes were modelled using SHERPA 2.2.1 at NLO accuracy in QCD for up to two parton emission and LO accuracy for up to four parton emission. The ME were calculated using the Comix and OpenLoops libraries [34]. Matching and merging were performed with the SHERPA parton shower scheme using the MEPS@NLO prescription. The NNPDF3.0NNLO PDF set was used, and the events are normalised to a prediction accurate to NNLO in QCD [71] for the inclusive production. The non-prompt events originating from the $t\bar{t}$ processes were modelled using the Powheg-Box v2 generator at NLO accuracy up to 2 parton emission and the NNPDF3.0NLO PDF set. The prediction was interfaced with PYTHIA 8.230 for modelling parton showering, hadronisation, and underlying events with parameters set according to the A14 tune.

The MC samples used in the BSM aNTGC interpretation of the CP study were generated at LO in QCD with MADGRAPH5_AMC@NLO 2.7.2 and interfaced with PYTHIA 8.244 for parton showering, hadronisation, and underlying-event, using a UFO model [72] as implemented in Ref. [28]. The aNTGC predictions are reweighted by applying a per-bin k-factor, derived by comparing the SHERPA prediction to the LO $q\bar{q} \to ZZ$ prediction in each bin of the OO to account for the missing higher-order effects in the BSM prediction.

The predictions from the MC simulations were passed through a detailed simulation of the ATLAS detector [73] based on Geant4 [74]. The effect of multiple pp interactions in the same bunch crossing, known as pile–up, was emulated by overlaying inelastic pp collisions, simulated with PYTHIA 8.186 using the NNPDF2.3LO set of PDFs and the A3 tune [75]. The events were then reweighted to match the distribution of the average number of interactions per bunch crossing observed in the data for different data-taking periods. The simulated events were reconstructed using the same algorithm used for the data.

Additionally, any efficiency discrepancies for the trigger, lepton reconstruction, identification, and isolation in MC events were corrected to match those measured in the data.

4 Fiducial region, object and event selections

4.1 Fiducial region definition

The fiducial phase space is defined close to the detector's kinematic acceptance using particle-level prompt[2] leptons produced by an MC event generator, without simulating the effects of the detector. The particle-level prompt leptons are *dressed* by adding the four-momenta of nearby prompt photons within a small $\Delta R < 0.1$ cone of the lepton's range. The dressed electrons (muons) are required to be within the detector's acceptance such that they satisfy $p_{\mathrm{T}} > 7$ (5) GeV and $|\eta| < 2.47$ (2.7). The fiducial phase space of the analysis does not include the prompt leptons from τ decays. Events must have a minimum of four prompt-dressed leptons to be grouped into at least two SFOC lepton pairs, and the leading and sub-leading leptons must have $p_{\mathrm{T}} > 20$ GeV. The angular separation between any two leptons is required to satisfy $\Delta R > 0.05$ to reduce the double counting of detector signatures while keeping leptons from possible boosted production scenarios. The invariant mass of any SFOC lepton pair is required to satisfy $m_{\ell\ell} > 5$ GeV.

An event quadruplet is formed from the two SFOC lepton pairs whose invariant masses are closest and next closest to m_Z. In the on-shell ZZ region, the resolution on m_Z is comparable to the mass difference between the two Z bosons, resulting in some events with inconsistent definitions of the leading and sub-leading pairs at particle and detector levels. This increases the resolution-induced bin migrations that need to be corrected for by the unfolding procedure. Therefore, once the quadruplet is formed, the leading (sub-leading)-lepton pair Z_1 (Z_2) is identified as the one with the larger (smaller) value of absolute rapidity, i.e., $y_{\ell\ell}$. Based on these requirements, the events are divided into three categories, $4e$ events with two e^+e^- pairs, 4μ events with two $\mu^+\mu^-$ pairs and $2e2\mu$ events where one of the pair is e^+e^- and the other is $\mu^+\mu^-$. The invariant mass of each SFOC lepton pair is required to be within $|m_{\ell\ell} - m_Z| < 10$ GeV, and the invariant mass of the four leptons is required to be $m_{4\ell} > 180$ GeV, motivated to select only on-shell ZZ events.

4.2 Object selection

Electrons are reconstructed by matching the topological energy clusters deposited in the electromagnetic calorimeters to the tracks in the ID [76]. The electron identification is based on a multivariate-likelihood technique that takes information on clusters' shower shapes in the electromagnetic calorimeters, ID track properties, and the quality of track-cluster matching. Electrons are calibrated using $Z \to e^+e^-$ events from data [77]. *Baseline* electrons, used for the non-prompt background estimation, are required to satisfy $p_{\mathrm{T}} > 7$ GeV, $|\eta| < 2.47$ and the 'VeryLoose' identification criteria [76] and loose association with the primary hard-scatter vertex by requiring $|z_0 \sin\theta| < 0.5$ mm, where z_0 is the z coordinate of the $r-\phi$ impact point. *Signal* electrons that define signal events are required to satisfy all of the baseline electron criteria as well as the stricter 'LooseBLayer' identification criteria and transverse impact parameter significance of $|d_0|/\sigma_{d_0} < 5$, where d_0 is the transverse impact parameter relative to the beamline, σ_{d_0} is its uncertainty.

[2] *prompt objects* are leptons and photons that do not originate from hadrons

Prompt leptons originating from hard scattering are characterised by low activity around them in the $\eta - \phi$ plane. Additionally, a signal electron must be isolated from other particles by applying criteria on the p_{T}-dependent isolation variable, which is defined using the electron's track and calorimeter energy deposits [77].

Muons are identified using information from various parts of the detector, the ID, the MS, and the calorimeters. A 'Loose' identification working point is used, which includes muon reconstructed from ID tracks identified as muons based on their calorimetric energy deposits or the presence of individual muon segments in the $|\eta| < 0.1$ region and the stand-alone MS tracks [78]. *Baseline* muons used in the non-prompt background estimation are required to pass the 'Loose' identification criteria, $p_{\mathrm{T}} > 5$ GeV, $|\eta| < 2.7$ and loose track to vertex association of $|z_0 \sin\theta| < 0.5$ mm. *Signal* muons are required to satisfy all criteria of baseline muons and transverse impact parameter significance of $|d_0|/\sigma_{d_0} < 3$. Similarly to the signal electrons, signal muons are required to satisfy additional isolation criteria on the p_{T}-dependent isolation variable, defined using the tracks and particle flow objects used in muon reconstruction [79].

Jets reconstructed using the anti-k_T algorithm with a distance parameter of $R = 0.4$ [80] are required to satisfy $p_{\mathrm{T}} > 15$ GeV and $|\eta| < 4.5$, and used in the non-prompt background estimation studies. Jets are reconstructed using the particle-flow algorithm, where energy deposited in the calorimeter by charged particles is subtracted and replaced by the momenta of tracks matched to those topological clusters [81]. In addition, b-jets are identified using a multivariate b-tagging algorithm [82]. The chosen b-tagging algorithm has an efficiency of 85% for b-jets and a rejection factor of 33 against light-flavour jets, which is measured in $t\bar{t}$ events [83].

An overlap removal is applied to avoid double-counting of the detector signal, favouring leptons with higher p_{T} and preferring non-calorimeter tagged muons over electrons if they share an ID track. The overlap removal rejects any jets within $\Delta R < 0.2$ of an electron or jets associated with less than three ID tracks if they overlap with a muon.

4.3 Event selection

The reconstructed events must have at least four baseline leptons, and the leading and sub-leading leptons must satisfy $p_{\mathrm{T}} > 20$ GeV. In each event, all possible SFOC lepton pairs are formed by requiring $m_{\ell\ell} > 5$ GeV and $\Delta R_{\ell\ell} > 0.05$ to suppress contributions from the leptonic decays of resonance hadrons. Like the fiducial region, a quadruplet is formed from two SFOC pairs with the highest values of $|m_{\ell\ell} - m_Z|$. The SFOC lepton pair with the largest value of $y_{\ell\ell}$ is defined as the leading Z-boson candidate. To ensure on-shell ZZ events, the invariant mass of the SFOC lepton pair is required to be $|m_{\ell\ell} - m_Z| < 10$ GeV and the invariant mass of the quadruplet is required to satisfy $m_{4\ell} > 180$ GeV. Each lepton of the quadruplet is required to pass the signal lepton definition for the signal region selection. Events with either one or more lepton in a quadruplet failing the signal lepton requirement are used in non-prompt background estimation.

5 Background estimation

After the event selection, the background consists of events with one or more of the reconstructed leptons in the quadruplet not originating from a Z boson decay. The background processes with prompt leptons from $t\bar{t}Z$ and fully leptonic decays of triboson processes are estimated using MC simulations. The measurement

also accounts for an additional source of background from non-prompt leptons originating from hadron decays, charge misidentification, or photon conversion. A data-driven *fake factor* method is used to estimate the non-prompt background.

A *fake factor* quantity, defined as the ratio of signal leptons to the number of baseline leptons failing the signal lepton criteria, is measured from data in dedicated control regions (CR) enriched with non-prompt leptons. The CR where the fake factors are evaluated consists of events with two prompt leptons from a physics process such as Z + jets or $t\bar{t}$ and additional leptons from other sources such as jets. The same triggers and object-level kinematic selections as in the signal region are also applied to select the CR events. The Z + jets CR is selected by requiring an SFOC signal lepton pair from a Z boson decay with an invariant mass of $76 < m_{\ell\ell} < 106$ GeV and additional baseline leptons. Similar to the signal region, SFOC lepton pairs are formed with leptons having $\Delta R > 0.05$ and $m_{\ell\ell} > 5$ GeV. Additionally, events are required to have a missing transverse energy less than 50 GeV to suppress the contamination from the WZ process. The $t\bar{t}$ CR is defined by requiring an SFOC signal lepton pair, at least one b-tagged jet and at least one additional baseline lepton.

The additional leptons in the Z + jets and $t\bar{t}$ CR originate predominantly from non-prompt sources such as heavy or light flavour jets and are used to derive the fake factors. The additional non-prompt leptons in Z + jets events arise dominantly from light-flavour jets, whereas they arise dominantly from heavy-flavour jets in $t\bar{t}$ events. To match the heavy-flavour composition in the signal region, the two types of events are first weighted and combined. The combination weight is evaluated by comparing the fraction of the non-prompt leptons from heavy-flavour decays in the Z + jets and $t\bar{t}$ events to that of the signal region events using the simulations discussed in Section 3. Since the compositions for the non-prompt electrons and muons are different in the signal region, the weights are evaluated separately to combine the control region events with additional baseline electrons and muons. When evaluating the fake factors, an estimate of the genuine baseline prompt leptons that fail the signal requirements from the WZ MC simulation are subtracted for both Z + jets and $t\bar{t}$ events. The fake factor is measured as a function of p_{T} and η of the non-prompt leptons as well as the number of jets in an event.

The non-prompt event yield in the signal region is then estimated by applying a fake factor weight to each baseline-not-signal lepton in events with a minimum of four baseline leptons and passing the same kinematic selection as in the signal region. Four-lepton events containing prompt baseline-not-signal leptons are removed from the estimation using simulations.

The background estimation is validated by comparing the prediction of the fake-factor method to the data in two dedicated validation regions where the non-prompt background events are expected to be dominant. The first one is the different-flavour validation region which has the same event selection requirements as the signal region but requires the leptons forming one of the pairs to have different flavours. The second one is the same-charge validation region, which requires the leptons in one of the pairs to have the same charge. In both validation regions, the data agree closely with the sum of the estimated non-prompt background yield and the MC prediction within the statistical uncertainties of the data.

Three sources of uncertainties in the background yield are considered. The first uncertainty is related to the statistics of the non-prompt leptons in the control region used to calculate the fake factors and ranges from 10 – 80%. The second set of uncertainty ranging from 2 – 40% is related to the theory uncertainties of the subtracted prompt-lepton component in the control region, which are dominated by the QCD scale variations. The third and dominant uncertainty ranging from 20 – 100% is the statistical precision on the number of events with at least four baseline leptons and at least one failing the signal lepton requirement.

6 Measurement methods

6.1 Polarisation measurements

The Z boson can be either transversely polarised or longitudinally polarised, and the polarisation fractions depend on the transverse momentum of the Z boson [84]. These effects lead to different kinematic properties of the production and the final decay states of the Z boson pair. From the reconstructed ZZ candidate events, in order to extract the fraction of $Z_{\mathrm{L}}Z_{\mathrm{L}}$ events, a multivariate technique based on a boosted decision tree (BDT) [85] is used to enhance the separation between $Z_{\mathrm{L}}Z_{\mathrm{L}}$ and $Z_{\mathrm{T}}Z_{\mathrm{X}}$ ($Z_{\mathrm{T}}Z_{\mathrm{T}}$ or $Z_{\mathrm{T}}Z_{\mathrm{L}}$) events. After a dedicated optimisation study to maximise the $Z_{\mathrm{L}}Z_{\mathrm{L}}$ signal sensitivity, input variables used in the BDT are the following: $\cos\theta_1$ ($\cos\theta_3$), where $\theta_1(\theta_3)$ is the angle between the negatively charged final-state lepton in the $Z_1(Z_2)$ rest frame and the direction of flight of the $Z_1(Z_2)$ boson in the four-lepton rest frame; $\cos\theta^*_{Z_1}$, where $\theta^*_{Z_1}$ is the production angle of the Z_1 defined in the four-lepton rest frame; $\Delta\phi_{\ell_1\ell_2}$ ($\Delta\phi_{\ell_3\ell_4}$), the azimuthal separation of the two leptons from $Z_1(Z_2)$ defined in the four-lepton rest frame. Definitions of the angles are illustrated in Figure 2. Other kinematic variables, such as the p_{T} and rapidity of Z_1 and Z_2 also have substantial separation power, but they are not included in the BDT training to reduce theoretical modelling uncertainties.

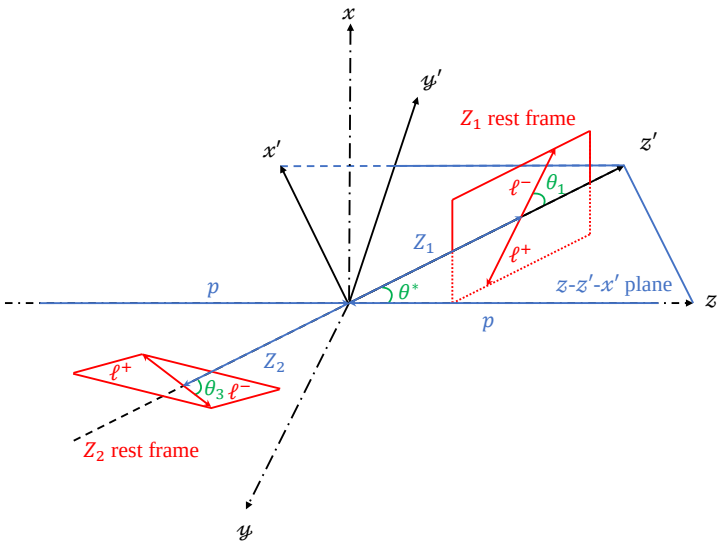

Figure 2: Definition of the angles used for the polarisation measurement and the reference frame used to define the CP-sensitive angles. The xyz-frame is the laboratory frame with the z-axis along the beam direction. The z'-axis is defined as the direction of motion of the Z_1 boson in the four-lepton rest frame. The x'-axis defines the reaction plane containing the laboratory z-axis and the z'-axis. The right-hand rule gives the y'-axis.

Higher-order corrections, in both QCD and EW, on MC templates of the different ZZ polarisation states have to be taken into account when extracting the $Z_{\mathrm{L}}Z_{\mathrm{L}}$ fraction from data. Recently the combined NLO QCD and EW corrections, as well as the loop-induced $gg \to ZZ$ corrections to the polarisation structure of ZZ production were calculated at the fixed-order with the MoCaNLO program [66]. Differential cross-sections for different polarisation states of the $q\bar{q} \to ZZ$ and $gg \to ZZ$ processes were provided for several kinematic observables. As in the simulated MC samples, the polarisation definition in the MoCaNLO program is also based on the CM frame of the two Z bosons. In order to incorporate the above

fixed-order higher-order corrections into the polarisation measurement, a three-step reweighting method is established, using either a one-dimensional (1D) observable or two-dimensional (2D) observables.

- **1D reweighting for each individual polarisation state.** In this step, the reweighting is done separately for the $q\bar{q} \to ZZ$ and $gg \to ZZ$ processes. For $q\bar{q} \to ZZ$, the combined NLO QCD and EW corrections as a function of the $\cos\theta_1$ variable are applied by taking the ratio of the differential cross-sections calculated from MoCaNLO at NLO and the ones from the MadGraph5_aMC@NLO MC samples at the particle level in the fiducial phase space of the measurement, for $Z_\mathrm{T}Z_\mathrm{T}$, $Z_\mathrm{T}Z_\mathrm{L}$ and $Z_\mathrm{L}Z_\mathrm{L}$ events, respectively. An additional reweighting as a function of $\cos\theta_1$ is applied to account for the missing higher-order QCD and parton shower effects by taking the ratio of unpolarised Sherpa $q\bar{q} \to ZZ$ predictions at the particle level to the unpolarised MoCaNLO calculations. The impact of these two 1D reweighting corrections on the BDT discriminant is mostly on the normalisation, about 20%, and the shape variation is 2 – 4%. For $gg \to ZZ$, which contributes to about 15% of the total signal yield, only the unpolarised MadGraph5_aMC@NLO MC sample at LO is available, and the MoCaNLO program provides polarised differential cross-sections at LO. Thus the unpolarised MadGraph5_aMC@NLO MC sample is reweighted to obtain polarised templates of $Z_\mathrm{T}Z_\mathrm{T}$, $Z_\mathrm{T}Z_\mathrm{L}$ and $Z_\mathrm{L}Z_\mathrm{L}$, by taking the fraction of polarised and unpolarised cross-sections calculated by MoCaNLO as a function of $\cos\theta_1$.
- **1D reweighting for the interference effect.** The simulated polarised samples does not consider the interference effects among different polarisation states, while such interference effects are found to be non-negligible in some kinematic regions where the contribution could reach up to 5% [66]. A dedicated template for the interference term is therefore constructed by reweighting the unpolarised Sherpa $q\bar{q} \to ZZ$ events with MoCaNLO calculations that include interference contributions, by taking the difference between the unpolarised cross-sections and the sum of the three polarised cross-sections as a function of $\cos\theta_1$. For $gg \to ZZ$ events, the interference effect is found to be negligible and thus ignored. For the subleading EW $qq \to ZZjj$ process, the interference effect is not included either.
- **2D reweighting for the residual higher-order corrections.** Four templates, including three polarisation states and the interference term, are obtained after the two reweighting steps described above. A closure test is performed by comparing the sum of the four templates and the prediction given by the unpolarised Sherpa MC events and residual discrepancies are observed, which could be due to the non-closure of the 1D reweighting method. An additional 2D reweighting is applied to each of the three polarisation templates to correct the mismodelling by taking the ratio of the non-closure effect and the sum of the three polarisation templates as a function of $\cos\theta^*_{Z_1}$ and $\Delta\phi_{\ell_1\ell_2}$. The impact of this 2D reweighting on the BDT discriminant is mostly on the shape with a variation of about 10%.

Figure 3 shows the BDT distribution of the three polarisation templates before and after the reweighting procedure. To extract the fraction of $Z_\mathrm{L}Z_\mathrm{L}$ events a profiled binned maximum-likelihood fit [86–88] to the BDT distribution is performed using the final templates for the three polarisation states and the interference term, and other non-ZZ background contributions. The normalisation factors of both the $Z_\mathrm{L}Z_\mathrm{L}$ template, the signal strength μ_{LL}, which is the ratio of the measured signal contribution relative to the SM expectation, and the combined $Z_\mathrm{T}Z_\mathrm{T} + Z_\mathrm{T}Z_\mathrm{L}$ templates, μ_{TX}, are allowed to float in the fit. A validation study is performed to demonstrate the robustness of the templates, by doing a similar fitting described above to the unpolarised Powheg Box MC events. The extracted $Z_\mathrm{L}Z_\mathrm{L}$ fraction is compared to the predicted $Z_\mathrm{L}Z_\mathrm{L}$ fraction, and they are found to be consistent within uncertainties.

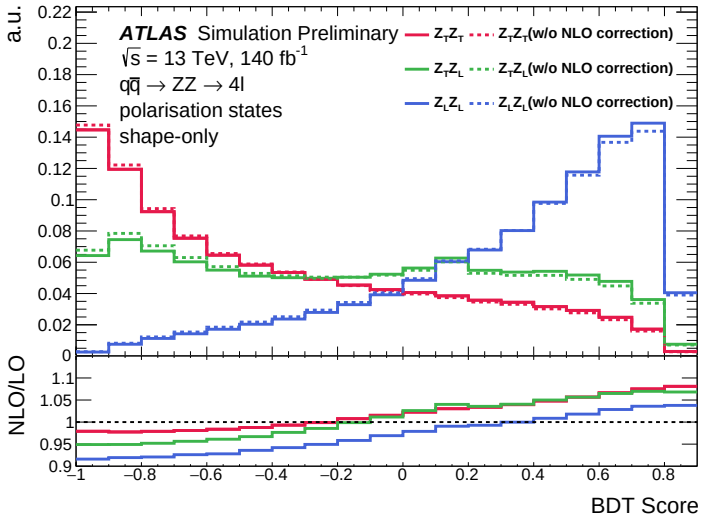

Figure 3: BDT distributions of the three polarisation templates for the $q\bar{q} \to ZZ$ process, before (dashed lines) and after (solid lines) the reweighting procedure to account for higher-order corrections. All distributions are normalised to the same area. The lower panel shows the ratio of the templates after the corrections to those before the corrections.

6.2 Study of CP property

6.2.1 CP-odd Optimal Observable

The OO defined for the CP study combines the CP-sensitive polar and azimuthal angles of both Z boson systems, providing additional CP sensitivity from shape differences between the SM and aNTGC predictions. The CP-sensitive polar angles $\theta_1(\theta_3)$ for the $Z_1(Z_2)$ boson are already defined in Section 6.1. The CP-sensitive azimuthal angles ϕ_1 and ϕ_3 are reconstructed in a reference frame that allows a direct measure of the Z boson spin as discussed in Ref. [24, 89] and are illustrated in Figure 2. The CP-sensitive azimuthal angle $\phi_1(\phi_3)$ is the azimuthal angle of the negative lepton in the $Z_1(Z_2)$ rest frame in this new axis system. The differential cross-sections for $\theta_1(\theta_3)$ and $\phi_1(\phi_3)$ are symmetric in the SM but asymmetric in the presence of the two CP-odd aNTGC.

To improve the sensitivity, the two CP-sensitive angles $\theta_1(\theta_3)$ and $\phi_1(\phi_3)$ are combined to form an angular observable $T_{yz,1(3)} = \sin\phi_{1(3)} \times \cos\theta_{1(3)}$ which maximises the asymmetry for each Z boson system. Figures 4(a) and 4(b) show the 2D differential distributions of the CP-sensitive observable T_{yz} of the two Z bosons, the symmetric SM prediction and asymmetric BSM prediction in the presence of a non-zero f_Z^4 parameter.

As observed in Figure 4(b), the first (bottom left) and the third (top right) quadrants where both Z bosons have negative and positive T_{yz} values, respectively, are the most sensitive regions of the 2D T_{yz} distribution. The OO $O_{T_{yz,1},T_{yz,3}}$ is defined from the $2D$ distribution of T_{yz} by grouping together the sensitive and non-sensitive bins to maximise the sensitivity for the four-lepton system. Each bin of the $O_{T_{yz,1},T_{yz,3}}$ observable represents approximately an L-shaped grouping of the bins around $T_{yz,3} = T_{yz,1}$ line as shown by Figure 5(a). The small fraction of events with miss-paired leptons in the $ZZ \to 4e$ (4μ) final states were studied and found to have negligible impact on the CP-sensitivity of the OO.

Figure 5(b) shows the measured data compared with the total SM signal and background MC prediction at the detector level of the OO $O_{T_{yz,1},T_{yz,3}}$. The bins 1 to 7 and 24 to 30 in Figure 5(b) represent the

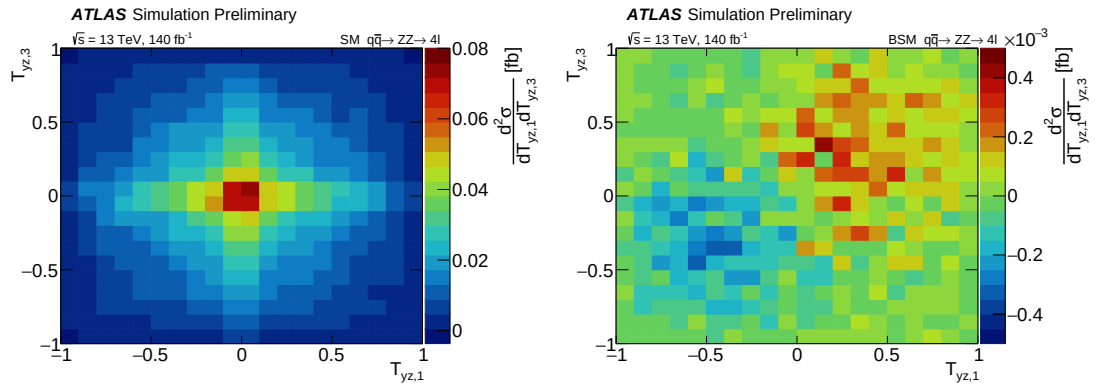

(a) (b)

Figure 4: Particle level 2D differential cross-sections of T_{yz} of the two Z bosons for the $q\bar{q} \to ZZ \to 4\ell$ process as predicted by (a) the SM and (b) in the presence of the BSM aNTGC vertex. The BSM prediction shows the linear only contribution when $f_Z^4 = 1$.

first quadrant and the third quadrant of the 2D distribution of $T_{yz,1}$ vs $T_{yz,3}$ shown in Figure 4. In these two quadrants, the T_{yz} observables for both Z bosons have the same sign in the SM and are the most CP-sensitive region, along with the two central bins representing the bin number 15 and 16 of the OO. The measured data agree closely with the prediction within the measurement's statistical precision and systematic uncertainties.

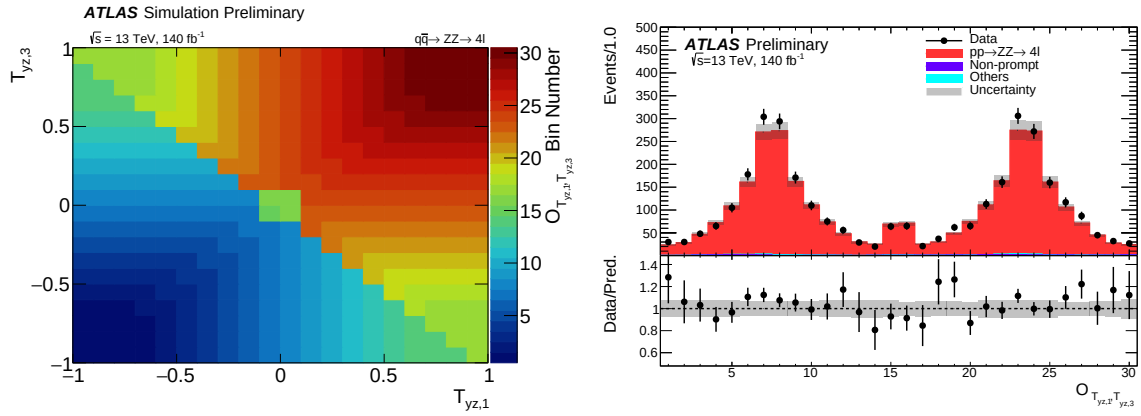

(a) (b)

Figure 5: The $2D \to 1D$ mapping (a) and (b) the detector level measurement of the Optimal Observable $O_{T_{yz,1},T_{yz,3}}$. The measured distribution is compared to the SM signal prediction and the total background. The 'Others' category includes the contribution from $t\bar{t}Z$ and VVZ processes. The non-prompt background is estimated using the fake-factor method. The grey band represents the effect of the total theoretical and experimental uncertainties for the detector-level predictions, and the vertical error bars on data represent the statistical uncertainties.

6.2.2 Detector corrections

Particle-level differential cross-sections for the on-shell ZZ production are obtained by correcting the detector effects such as inefficiency and resolution. The background-subtracted event yields are corrected using an iterative Bayesian unfolding method [90].

The first step of the correction multiplies each bin yield by a fiducial correction factor obtained from the SHERPA SM prediction, which accounts for the events that pass the detector level but fail the fiducial-level event selections. This correction accounts for the $5-20\%$ of the fake fiducial events in various bins caused by the resolution effects that enter the detector-level event selection. Then, the detector resolution-induced bin migration is corrected iteratively using the SM particle-level distribution as the initial prior. With an increasing number of iterations, the statistical uncertainty increases, and the residual bias with respect to the prior decreases due to the improvement of its knowledge. Two iterations were deemed optimal as a compromise between the increasing statistical uncertainty and decreasing bias. The final step in the unfolding procedure is to correct for the detector inefficiency by dividing the per bin yield by the ratio of the number of events passing both particle- and reconstruction-level selections to the number passing the particle-level selections.

A data-driven closure test is performed to evaluate the model dependence of the unfolding method. This test first simulates a pseudo-data sample by reweighting the SM prediction to the shape observed in the data. The pseudo dataset is then unfolded using the nominal SM prediction. The comparison of the unfolded pseudo-dataset with the reweighted particle-level prediction gives the intrinsic bias of the unfolding method, which was found to be less than 1% in each bin of the unfolded $O_{T_{yz,1},T_{yz,3}}$ observable in the case of two iterations of unfolding. This resulting bias is taken as a systematic uncertainty of the final result. Moreover, the uncertainty related to the choice of the generator in the unfolding is studied using the alternative POWHEG prediction of the $q\bar{q} \to ZZ$ process, which is reweighted to match the nominal SHERPA lineshape to avoid double counting of the data-driven bias. The generator bias estimated by comparing the difference in the unfolded results is negligible.

Additionally, an injection test is performed to evaluate the robustness of the unfolding algorithm in the presence of BSM physics in the data. A detector-level distribution for the BSM aNTGC parameter $f_4^Z = 1$ is injected into the SM detector-level prediction. The BSM-injected detector level distribution is then unfolded using the inputs from the nominal SM prediction. When compared, the unfolded distribution agrees closely with the corresponding particle level distribution within uncertainties.

7 Systematic uncertainties

Both the polarisation and CP property study presented here are affected by some common sources of theoretical, experimental and background-related uncertainties.

Theoretical systematic uncertainties affecting the results of this analysis arise from three sources, uncertainties related to the QCD scale dependence, uncertainties related to the choice of the PDF, and uncertainties related to the higher-order corrections. The impact of each source of these systematics is propagated to the final results. The QCD scale dependency is evaluated individually for three physics processes $q\bar{q} \to ZZ$, $gg \to ZZ$, and the EW $qq \to ZZjj$ by varying the default choice of renormalisation and factorisation scales independently by factors of two and one-half, removing combinations where the

variations differ by a factor of four. The envelope of the effects from these variations is taken as the final scale uncertainty for each process individually.

The PDF-related uncertainty for each of these samples is estimated using the PDF4LHC recommendation [91]. The PDF variations include a set of 100 replica variations on the nominal NNPDF set, two additional variations from the nominal PDF reweighted to the alternative MMHT2014nnlo [92], and CT14nnlo [93] PDF sets and variations of the strong coupling constant by ±0.001 around the nominal value of $\alpha_S = 0.118$. The total PDF uncertainty is the absolute envelope of standard deviations of 100 internal variations and the two alternate PDF variations, added in quadrature with the envelope of the α_S variations.

For the polarisation measurements, dedicated systematic uncertainties are considered in the modelling of the polarisation templates, including theoretical uncertainties from higher-order corrections, PDFs and α_S described above, and the uncertainties associated with the reweighting methods as described in Section 6.1. For both the $q\bar{q} \to ZZ$ and $gg \to ZZ$ polarisation templates, the theoretical uncertainties from QCD scales are taken from the MoCaNLO calculations by varying the QCD scales as described above, while for the template of the interference term, which is reweighted from the unpolarised Sherpa $q\bar{q} \to ZZ$ samples, these theoretical uncertainties are estimated from the Sherpa sample. The parton showering and hadronisation uncertainty is estimated for the signal by comparing the nominal Pythia 8 parton showering with the alternative Herwig 7 [94, 95] algorithm. Uncertainties from the NLO EW corrections are estimated by taking the difference between the additive and the multiplicative prescription in MoCaNLO [66]. For the 1D reweighting method in Section 6.1, the uncertainty is estimated by comparing the reweighted templates using the nominal observable and an alternative observable, the rapidity difference of the two Z bosons. For the additional 2D reweighting, the residual difference between the sum of the four templates and the unpolarised prediction from the Sherpa sample is taken as an uncertainty.

For the CP study, additional uncertainties associated with the higher-order corrections applied to the inclusive $q\bar{q} \to ZZ$ and $gg \to ZZ$ samples are considered. For the virtual NLO electroweak effects on $q\bar{q} \to ZZ$, a 100% uncertainty was assigned to the reweighting function to account for non-factorising effects in events with high QCD activity [96]. The uncertainty on the NLO QCD k-factors for the $gg \to ZZ$ is evaluated differentially as a function of the $m_{4\ell}$ as discussed in Ref. [58].

The **experimental uncertainties** associated with reconstruction, identification, isolation and track-to-vertex matching efficiencies, and momentum resolution and scale of the leptons are dominant and originate from imperfect modelling in the simulation and uncertainties in the determination of the correction factors. The uncertainties associated with each scale factor that is applied in the simulation are estimated by modifying the nominal values by their associated uncertainties [76, 78].

An uncertainty of ±0.83% from the measurement of Run-2 dataset luminosity [97] is propagated to the final results. A systematic uncertainty related to the pile-up reweighting is included to cover the uncertainty in the ratio of the predicted and measured pp inelastic cross-sections [98].

The **background related uncertainties** are from two distinct sources, uncertainties related to the non-prompt background estimation, discussed in Section 5, and the uncertainty related to the background containing four prompt leptons simulated from MC. The simulation of $t\bar{t}Z$ and triboson background processes are normalised to ATLAS measurements, as outlined in Section 3, and the uncertainty related is estimated by varying the normalisation of the simulated samples by the experimental precision of the ATLAS measurements.

For the CP study, the systematic uncertainties are propagated to the particle level through the unfolding method. The effect of each systematic source is evaluated using simulation. Since the theory variation applied affects both the detector and the particle-level yields, the resulting uncertainties from theory systematics on the unfolded cross-sections are minor. Another source of systematic uncertainty related to the intrinsic unfolding bias discussed in Section 6.2.2 is also included in the differential cross-sections and the BSM interpretation.

8 Results

8.1 Polarisation measurements

The profiled likelihood fitting procedure described in Section 6.1 is performed to the BDT distribution of the data. Systematic uncertainties described in the above section are modelled as Gaussian-constrained nuisance parameters in the likelihood. Figure 6 shows the post-fit BDT distribution in the signal region. The corresponding pre-fit and post-fit yields in the signal region are detailed in Table 1. The decrease of the yield uncertainty for $Z_{\mathrm{T}}Z_{\mathrm{T}}$ is mainly due to the constraint on the normalisation from the fit and the increase of the yield uncertainty for $Z_{\mathrm{L}}Z_{\mathrm{L}}$ is mainly due to the statistical uncertainty of the signal strength after the fit. The $Z_{\mathrm{L}}Z_{\mathrm{L}}$ signal strength is measured to be $\mu_{LL} = 1.16 \pm 0.26(\mathrm{stat.}) \pm 0.11(\mathrm{syst.}) = 1.16 \pm 0.28$, where the uncertainties are either statistical (stat.) or of systematic (syst.) nature. This corresponds to a significance of 4.3 standard deviations. Figure 7 shows the profile likelihood ratio [99] as a function of μ_{LL}. The measured results are consistent with the SM expectation of $\mu_{LL} = 1.00 \pm 0.28$ with a significance of 3.8σ. The normalisation factor for the $Z_{\mathrm{T}}Z_{\mathrm{X}}$ template is measured to be $\mu_{TX} = 0.99 \pm 0.05$, also consistent with the SM prediction.

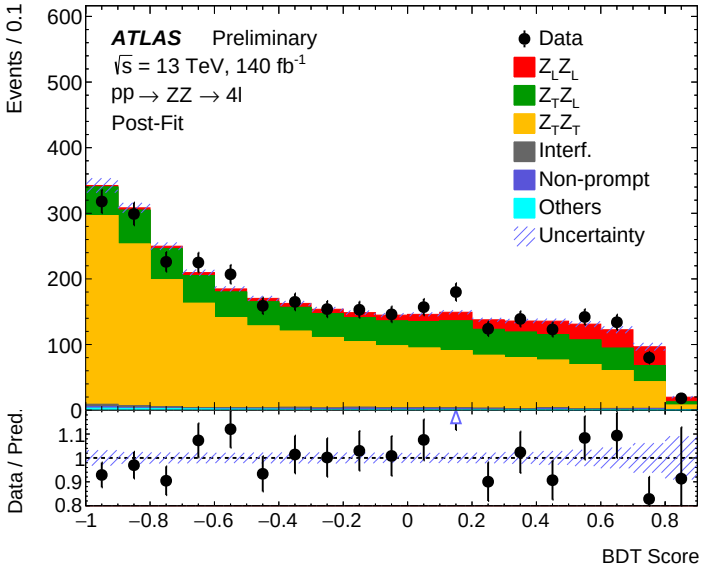

Figure 6: The BDT distribution of the data and the post-fit SM predictions. The 'Others' category represents the contribution from $t\bar{t}Z$ and VVZ. The lower panel shows the ratio of the data points to the post-fit total prediction. The arrow indicates that the ratio lies outside the range covered by the vertical axis. The uncertainty bands include both the statistical and systematic uncertainties as obtained by the fit.

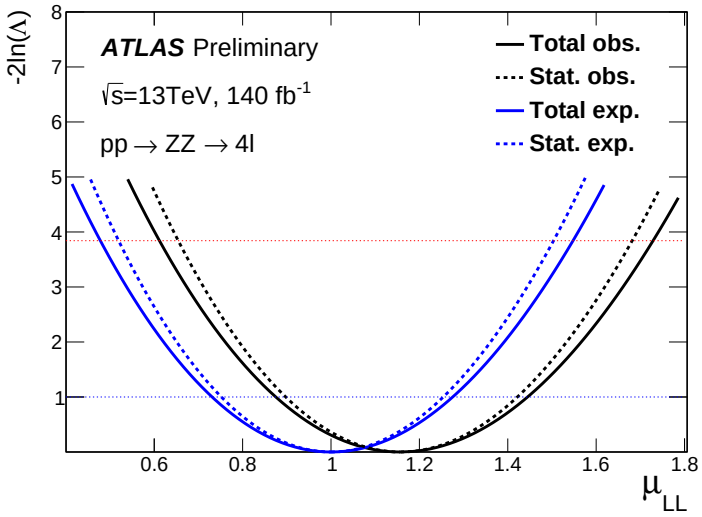

Figure 7: Observed and expected profile likelihood ratio, $-2\ln\Lambda$, as a function of the signal strength μ_{LL}, with (solid curves) and without (dashed curves) systematic uncertainties included.

Table 1: Expected and observed numbers of events in the signal region. Numbers are presented before and after the fit to the BDT distribution. The 'Others' category represents the contribution from $t\bar{t}Z$ and VVZ. For the $Z_{\mathrm{L}}Z_{\mathrm{L}}$ signal, the pre-fit yield values correspond to the theoretical prediction and corresponding uncertainties. The uncertainties include both the statistical and systematic contributions. The uncertainty in the total yield can be smaller than the quadrature sum of the contributions because of correlations resulting from the fit.

		Pre-fit	Post-fit
ZZ	$Z_{\mathrm{L}}Z_{\mathrm{L}}$	189.1 ± 8.8	220 ± 53
	$Z_{\mathrm{T}}Z_{\mathrm{L}}$	710 ± 29	711 ± 29
	$Z_{\mathrm{T}}Z_{\mathrm{T}}$	2170 ± 120	2146 ± 60
	Interference	34.2 ± 3.1	33.8 ± 2.9
Non-prompt		18.7 ± 7.1	18.5 ± 7.0
Others		20.0 ± 3.7	19.9 ± 3.7
Total		3140 ± 150	3149 ± 57
Data		3149	3149

An additional profiled likelihood fit is performed to convert the measured μ_{LL} to the measured fiducial cross-section, with the normalisation effects from the theoretical uncertainties of the $Z_{\mathrm{L}}Z_{\mathrm{L}}$ template removed. The fiducial cross-section of the $Z_{\mathrm{L}}Z_{\mathrm{L}}$ production is measured to be $\sigma^{\mathrm{obs.}}_{Z_{\mathrm{L}}Z_{\mathrm{L}}} = 2.44 \pm 0.55(\mathrm{stat.}) \pm 0.21(\mathrm{syst.})$ fb = 2.44 ± 0.59 fb, consistent with the SM prediction of $\sigma^{\mathrm{pred.}}_{Z_{\mathrm{L}}Z_{\mathrm{L}}} = 2.09 \pm 0.10$ fb. The SM prediction includes NLO QCD and EW corrections for the $q\bar{q} \to ZZ$ process, the LO prediction for the $gg \to ZZ$ process, both of which are calculated from MoCaNLO, and the LO prediction for the EW $qq \to ZZjj$ process. The uncertainty mainly includes the QCD scale and PDF uncertainties. The measurement is limited by data statistics and the impact of uncertainties on the measured $Z_{\mathrm{L}}Z_{\mathrm{L}}$ fiducial cross-section is shown in Table 2, with the leading contribution from the theoretical modelling of the polarisation templates.

Table 2: Impact of uncertainties on the measured fiducial cross-section $\sigma_{Z_L Z_L}$ from the fit. The impact from a group of nuisance parameters is defined via quadrature subtraction of the $\sigma_{Z_L Z_L}$ uncertainties: $\sqrt{\Delta\sigma^2 - \Delta\sigma'^2}$, where $\Delta\sigma$ is the uncertainty of the $\sigma_{Z_L Z_L}$ from the nominal fit and the $\Delta\sigma'$ is the uncertainty of the $\sigma_{Z_L Z_L}$ when this group of nuisance parameters are fixed to their best-fit values from the nominal fit.

Contribution	Relative uncertainty [%]
Total	24
Data statistics	23
Total systematics	8.5
MC statistics	1.7
Theoretical uncertainties	
$q\bar{q} \to ZZ$ interference modelling	7.1
NLO reweighting observable choice for $q\bar{q} \to ZZ$	3.7
NLO reweighting non-closure	1.7
PDF, α_s and parton shower for $q\bar{q} \to ZZ$	0.5
QCD scale for $q\bar{q} \to ZZ$	0.3
NLO EW corrections for $q\bar{q} \to ZZ$	0.1
$gg \to ZZ$ modelling	1.3
Experimental systematic uncertainties	
Luminosity	0.8
Muon related uncertainties	0.6
Electron related uncertainties	0.4
Non-prompt background	0.4
Pile-up reweighting	0.4
Triboson and $t\bar{t}Z$	0.2

8.2 Unfolded differential measurement

The differential cross-section for the $ZZ \to 4\ell$ production as a function of the OO $O_{T_{yz,1},T_{yz,3}}$ is shown in Figure 8 and compared to the SM prediction, where $q\bar{q} \to ZZ$ predictions are taken from the Sherpa generator. The vertical error bars on data represent the statistical uncertainty. In contrast, the band represents the total uncertainties, which are small and flat, related to the theoretical, experimental and unfolding procedure-related uncertainties on the unfolded differential cross-section. Similarly, for the SM prediction, the uncertainty band represents the total theoretical uncertainties on the total SM prediction. For each bin, the predicted cross-section agrees closely with the cross-section measured from the data.

8.3 BSM interpretation

The differential cross-section as a function of $O_{T_{yz,1},T_{yz,3}}$ and the corresponding aNTGC prediction are used to define a likelihood function,

$$\mathcal{L} = \frac{1}{\sqrt{(2\pi)^k\,|C|}} \exp\left\{-\frac{1}{2}\left[\vec{\sigma}^{\text{meas.}} - \vec{\sigma}^{\text{pred.}}\left(\vec{\theta}\right)\right]^T C^{-1}\left[\vec{\sigma}^{\text{meas.}} - \vec{\sigma}^{\text{pred.}}\left(\vec{\theta}\right)\right]\right\} \times \prod_i \mathcal{G}\left(\theta_i, 0, 1\right) , \quad (2)$$

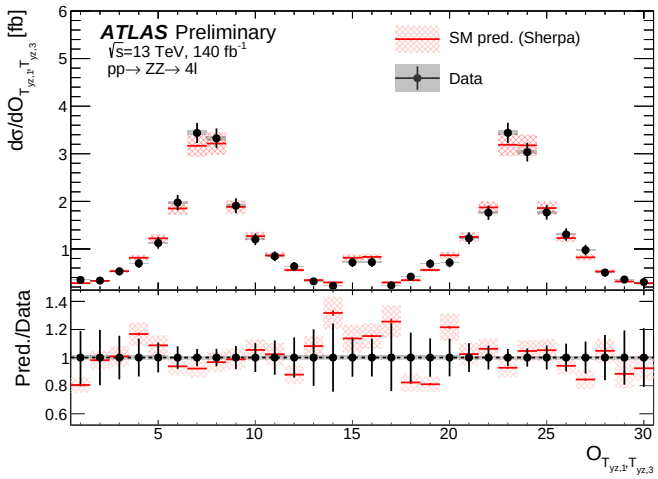

Figure 8: Unfolded differential cross-section as a function of the Optimal Observable $O_{T_{yz,1},T_{yz,3}}$. The grey and red uncertainty bands represent the respective systematic uncertainties in the measured unfolded cross-section and predicted particle-level cross-section. The vertical error bars represent the statistical uncertainties on the measured differential cross-section.

where $\vec{\sigma}^{\text{meas.}}$ and $\vec{\sigma}^{\text{pred.}}$ are the measured and predicted differential cross-section as a function of $O_{T_{yz,1},T_{yz,3}}$, respectively, and C is the total covariance matrix defined by the sum of the statistical and systematic covariances in $\vec{\sigma}^{\text{meas.}}$ and $\vec{\sigma}^{\text{pred.}}$. Each systematic uncertainty is treated as fully correlated across bins but uncorrelated with other uncertainty sources. Each source of theoretical uncertainty affecting the SM particle level prediction of the $q\bar{q} \to ZZ$, $gg \to ZZ$ and EW $qq \to ZZjj$ processes is implemented as nuisance parameters, $\vec{\theta}$, with Gaussian constraints, $\mathcal{G}(\theta_i, 0, 1)$.

Limits are set on CP-odd aNTGC parameters in two scenarios, with linear interference terms only and with quadratic terms included. For each CP-odd aNTGC parameter under test, the other is set to zero, and the test statistics are constructed based on the ratio of profiled likelihoods [99],

$$q = -2 \ln \frac{\mathcal{L}(c, \hat{\hat{\vec{\theta}}}(c))}{\mathcal{L}(\hat{c}, \hat{\hat{\vec{\theta}}}(c))}, \tag{3}$$

where c is the aNTGC parameter, $\hat{c}$ and $\hat{\vec{\theta}}$ are the unconditional maximum-likelihood estimators, and $\hat{\hat{\vec{\theta}}}(c)$ is the conditional maximum likelihood estimated under the c hypothesis.

Using the test statistic in Eq. 3, which is assumed to be distributed according to a χ^2 distribution with one degree of freedom following the Wilks' theorem [100], a 95% confidence level for each aNTGC parameter is calculated, as shown in Table 3. Theoretical uncertainties related to the QCD scale, PDF, α_S, and parton showering for the $q\bar{q} \to ZZ$ predictions have the largest impact on the estimated confidence interval.

From Table 3, the constraints on the CP-odd f_Z^4 and f_γ^4 aNTGC parameters using the linear interference term when the quadratic term is set to zero are much worse than those obtained using high-p_{T} kinematic observables with quadratic terms included [23], as expected. However, these are the first constraints on CP-odd aNTGC parameters using only linear interference terms with a dedicated CP-sensitive OO, based on angular observables. Additional likelihood fits are performed with the quadratic terms included, and the constraints on f_Z^4 and f_γ^4 are improved by one order of magnitude, but since $O_{T_{yz,1},T_{yz,3}}$ is not sensitive

to the high-p_{T} regime, such constraints are still not tighter than those obtained with high-p_{T} kinematic observables.

Table 3: Expected and observed 95% confidence interval for the two aNTGC operators using the measured particle-level differential cross-section as a function of $O_{T_{yz,1},T_{yz,3}}$. For the 'Full' case, both the interference and the quadratic terms are included in the aNTGC prediction.

aNTGC parameter	Interference only		Full	
	Expected	Observed	Expected	Observed
f_Z^4	$[-0.16, 0.16]$	$[-0.12, 0.20]$	$[-0.013, 0.012]$	$[-0.012, 0.012]$
f_γ^4	$[-0.30, 0.30]$	$[-0.34, 0.28]$	$[-0.015, 0.015]$	$[-0.015, 0.015]$

9 Conclusion

Studies of the polarisation and CP properties in $ZZ \to 4\ell$ production are presented for the first time, using proton–proton collisions at the LHC collected with the ATLAS detector at $\sqrt{s} = 13$ TeV with an integrated luminosity of 140 fb^{-1}. The Z boson candidates are reconstructed with same-flavour, opposite-charge electron or muon pairs, and they are required to be on-shell with $|m_{\ell\ell} - m_Z| < 10$ GeV. The production of two simultaneously longitudinally polarised Z bosons is measured with observed and expected significances of 4.3 and 3.8 standard deviations, respectively. The production cross-section of $Z_{\mathrm{L}}Z_{\mathrm{L}}$ events is measured in a fiducial phase space as 2.44 ± 0.59 fb, consistent with the Standard Model prediction of 2.09 ± 0.10 fb with NLO QCD and EW corrections considered. Differential cross-section of the inclusive ZZ production as a function of a CP-sensitive angular observable, $O_{T_{yz,1},T_{yz,3}}$, is also measured. Furthermore, the measured differential cross-section is used to constrain CP-odd neutral triple gauge couplings, f_Z^4 and f_γ^4. No significant deviations from the SM are observed.

References

[1] D. Liu and L.-T. Wang, *Prospects for precision measurement of diboson processes in the semileptonic decay channel in future LHC runs*, Phys. Rev. D **99** (2019) 055001, arXiv: 1804.08688 [hep-ph] (cit. on p. 2).

[2] CMS Collaboration, *Measurement of the Polarization of W Bosons with Large Transverse Momenta in W+Jets Events at the LHC*, Phys. Rev. Lett. **107** (2011) 021802, arXiv: 1104.3829 [hep-ex] (cit. on p. 2).

[3] ATLAS Collaboration, *Measurement of the polarisation of W bosons produced with large transverse momentum in pp collisions at $\sqrt{s} = 7$ TeV with the ATLAS experiment*, Eur. Phys. J. C **72** (2012) 2001, arXiv: 1203.2165 [hep-ex] (cit. on p. 2).

[4] ATLAS Collaboration, *Measurement of the angular coefficients in Z-boson events using electron and muon pairs from data taken at $\sqrt{s} = 8$ TeV with the ATLAS detector*, JHEP **08** (2016) 159, arXiv: 1606.00689 [hep-ex] (cit. on p. 2).

[5] CMS Collaboration, *Angular coefficients of Z bosons produced in pp collisions at $\sqrt{s} = 8$ TeV and decaying to $\mu^+\mu^-$ as a function of transverse momentum and rapidity*, Phys. Lett. B **750** (2015) 154, arXiv: 1504.03512 [hep-ex] (cit. on p. 2).

[6] ATLAS Collaboration, *Measurement of the W boson polarisation in $t\bar{t}$ events from pp collisions at $\sqrt{s} = 8$ TeV in the lepton+jets channel with ATLAS*, Eur. Phys. J. C **77** (2017) 264, arXiv: 1612.02577 [hep-ex] (cit. on p. 2), Erratum: Eur. Phys. J. C **79** (2019) 19.

[7] CMS Collaboration, *Measurement of the W boson helicity fractions in the decays of top quark pairs to lepton+jets final states produced in pp collisions at $\sqrt{s} = 8$ TeV*, Phys. Lett. B **762** (2016) 512, arXiv: 1605.09047 [hep-ex] (cit. on p. 2).

[8] ATLAS and CMS Collaborations, *Combination of the W boson polarization measurements in top quark decays using ATLAS and CMS data at $\sqrt{s} = 8$ TeV*, JHEP **08** (2020) 051, arXiv: 2005.03799 [hep-ex] (cit. on p. 2).

[9] ATLAS Collaboration, *Measurement of $W^\pm Z$ production cross sections and gauge boson polarisation in pp collisions at $\sqrt{s} = 13$ TeV with the ATLAS detector*, Eur. Phys. J. C **79** (2019) 535, arXiv: 1902.05759 [hep-ex] (cit. on p. 2).

[10] CMS Collaboration, *Measurement of the inclusive and differential WZ production cross sections, polarization angles, and triple gauge couplings in pp collisions at $\sqrt{s} = 13$ TeV*, JHEP **07** (2021) 032, arXiv: 2110.11231 [hep-ex] (cit. on p. 2).

[11] CMS Collaboration, *Measurements of production cross sections of polarized same-sign W boson pairs in association with two jets in proton–proton collisions at $\sqrt{s} = 13$ TeV*, Phys. Lett. B **812** (2021) 136018, arXiv: 2009.09429 [hep-ex] (cit. on p. 2).

[12] ATLAS Collaboration, *Observation of gauge boson joint-polarisation states in $W^\pm Z$ production from pp collisions at $\sqrt{s} = 13$ TeV with the ATLAS detector*, (2022), arXiv: 2211.09435 [hep-ex] (cit. on p. 2).

[13] R. L. Workman et al., *Review of Particle Physics*, PTEP **2022** (2022) 083C01 (cit. on p. 2).

[14] M. B. Gavela, P. Hernández, J. Orloff and O. Pène, *Standard model CP violation and baryon asymmetry*, Mod. Phys. Lett. A **9** (1994) 795, arXiv: hep-ph/9312215 (cit. on p. 2).

[15] A. G. Cohen, D. B. Kaplan and A. E. Nelson, *Progress in Electroweak Baryogenesis*, Ann. Rev. Nucl. Part. Sci. **43** (1993) 27, arXiv: hep-ph/9302210 (cit. on p. 2).

[16] P. Huet and E. Sather, *Electroweak baryogenesis and standard model CP violation*, Phys. Rev. D **51** (1995) 379, arXiv: hep-ph/9404302 (cit. on p. 2).

[17] ATLAS Collaboration, *Measurement of ZZ production in pp collisions at $\sqrt{s} = 7$ TeV and limits on anomalous ZZZ and $ZZ\gamma$ couplings with the ATLAS detector*, JHEP **03** (2013) 128, arXiv: 1211.6096 [hep-ex] (cit. on p. 2).

[18] ATLAS Collaboration, *Measurement of the ZZ production cross section in proton–proton collisions at $\sqrt{s} = 8$ TeV using the $ZZ \to \ell^-\ell^+\ell'^-\ell'^+$ and $ZZ \to \ell^-\ell^+\nu\bar{\nu}$ decay channels with the ATLAS detector*, JHEP **01** (2017) 099, arXiv: 1610.07585 [hep-ex] (cit. on p. 2).

[19] ATLAS Collaboration, *Measurement of ZZ production in the $\ell\ell\nu\nu$ final state with the ATLAS detector in pp collisions at $\sqrt{s} = 13$ TeV*, JHEP **10** (2019) 127, arXiv: 1905.07163 [hep-ex] (cit. on p. 2).

[20] ATLAS Collaboration, *$ZZ \to \ell^+\ell^-\ell'^+\ell'^-$ cross-section measurements and search for anomalous triple gauge couplings in 13 TeV pp collisions with the ATLAS detector*, Phys. Rev. D **97** (2018) 032005, arXiv: 1709.07703 [hep-ex] (cit. on p. 2).

[21] CMS Collaboration, *Measurement of the $pp \to ZZ$ production cross section and constraints on anomalous triple gauge couplings in four-lepton final states at $\sqrt{s} = 8$ TeV*, Phys. Lett. B **740** (2015) 250, arXiv: 1406.0113 [hep-ex], Erratum: Phys. Lett. B **757**, 569–569 (2016) (cit. on p. 2).

[22] CMS Collaboration, *Measurements of the ZZ production cross sections in the $2\ell 2\nu$ channel in proton–proton collisions at $\sqrt{s} = 7$ and 8 TeV and combined constraints on triple gauge couplings*, Eur. Phys. J. C **75** (2015) 511, arXiv: 1503.05467 [hep-ex] (cit. on p. 2).

[23] CMS Collaboration, *Measurements of $pp \to ZZ$ production cross sections and constraints on anomalous triple gauge couplings at $\sqrt{s} = 13$ TeV*, Eur. Phys. J. C **81** (2021) 200, arXiv: 2009.01186 [hep-ex] (cit. on pp. 2, 18).

[24] R. Rahaman and R. K. Singh, *On polarization parameters of spin-1 particles and anomalous couplings in $e^+e^- \to ZZ/Z\gamma$*, Eur. Phys. J. C **76** (2016) 539, arXiv: 1604.06677 [hep-ph] (cit. on pp. 3, 11).

[25] R. Rahaman and R. K. Singh, *Anomalous triple gauge boson couplings in ZZ production at the LHC and the role of Z boson polarizations*, Nucl. Phys. B **948** (2019) 114754, arXiv: 1810.11657 [hep-ph] (cit. on p. 3).

[26] G. J. Gounaris, J. Layssac and F. M. Renard, *Signatures of the anomalous $Z\gamma$ and ZZ production at lepton and hadron colliders*, Phys. Rev. D **61** (2000) 073013, arXiv: hep-ph/9910395 (cit. on p. 3).

[27] ATLAS Collaboration, *Differential cross-section measurements for the electroweak production of dijets in association with a Z boson in proton–proton collisions at ATLAS*, Eur. Phys. J. C **81** (2021) 163, arXiv: 2006.15458 [hep-ex] (cit. on p. 3).

[28] A. Biekötter, P. Gregg, F. Krauss and M. Schönherr, *Constraining CP violating operators in charged and neutral triple gauge couplings*, Phys. Lett. B **817** (2021) 136311, arXiv: 2102.01115 [hep-ph] (cit. on pp. 3, 5).

[29] ATLAS Collaboration, *The ATLAS Experiment at the CERN Large Hadron Collider*, JINST **3** (2008) S08003 (cit. on p. 3).

[30] ATLAS Collaboration, *The ATLAS Collaboration Software and Firmware*, ATL-SOFT-PUB-2021-001, 2021, URL: https://cds.cern.ch/record/2767187 (cit. on p. 3).

[31] ATLAS Collaboration, *Performance of electron and photon triggers in ATLAS during LHC Run 2*, Eur. Phys. J. C **80** (2020) 47, arXiv: 1909.00761 [hep-ex] (cit. on p. 4).

[32] ATLAS Collaboration, *Performance of the ATLAS muon triggers in Run 2*, JINST **15** (2020) P09015, arXiv: 2004.13447 [hep-ex] (cit. on p. 4).

[33] E. Bothmann et al., *Event Generation with Sherpa 2.2*, SciPost Phys. **7** (2019) 034, arXiv: 1905.09127 [hep-ph] (cit. on p. 4).

[34] T. Gleisberg and S. Höche, *Comix, a new matrix element generator*, JHEP **12** (2008) 039, arXiv: 0808.3674 [hep-ph] (cit. on pp. 4, 5).

[35] S. Schumann and F. Krauss, *A parton shower algorithm based on Catani–Seymour dipole factorisation*, JHEP **03** (2008) 038, arXiv: 0709.1027 [hep-ph] (cit. on p. 4).

[36] S. Höche, F. Krauss, M. Schönherr and F. Siegert, *A critical appraisal of NLO+PS matching methods*, JHEP **09** (2012) 049, arXiv: 1111.1220 [hep-ph] (cit. on p. 4).

[37] S. Catani, F. Krauss, B. R. Webber and R. Kuhn, *QCD Matrix Elements + Parton Showers*, JHEP **11** (2001) 063, arXiv: hep-ph/0109231 (cit. on pp. 4, 5).

[38] S. Höche, F. Krauss, M. Schönherr and F. Siegert, *QCD matrix elements + parton showers: The NLO case*, JHEP **04** (2013) 027, arXiv: 1207.5030 [hep-ph] (cit. on pp. 4, 5).

[39] F. Cascioli, P. Maierhöfer and S. Pozzorini, *Scattering Amplitudes with Open Loops*, Phys. Rev. Lett. **108** (2012) 111601, arXiv: 1111.5206 [hep-ph] (cit. on p. 4).

[40] F. Buccioni et al., *OpenLoops 2*, Eur. Phys. J. C **79** (2019) 866, arXiv: 1907.13071 [hep-ph] (cit. on p. 4).

[41] A. Denner, S. Dittmaier and L. Hofer, *Collier: A fortran-based complex one-loop library in extended regularizations*, Comput. Phys. Commun. **212** (2017) 220, arXiv: 1604.06792 [hep-ph] (cit. on p. 4).

[42] The NNPDF Collaboration, R. D. Ball et al., *Parton distributions for the LHC run II*, JHEP **04** (2015) 040, arXiv: 1410.8849 [hep-ph] (cit. on p. 4).

[43] B. Biedermann, A. Denner, S. Dittmaier, L. Hofer and B. Jäger, *Electroweak corrections to $pp \to \mu^+\mu^-e^+e^- + X$ at the LHC: a Higgs background study*, Phys. Rev. Lett. **116** (2016) 161803, arXiv: 1601.07787 [hep-ph] (cit. on p. 4).

[44] B. Biedermann, A. Denner, S. Dittmaier, L. Hofer and B. Jager, *Next-to-leading-order electroweak corrections to the production of four charged leptons at the LHC*, JHEP **01** (2017) 033, arXiv: 1611.05338 [hep-ph] (cit. on p. 4).

[45] S. Alioli, P. Nason, C. Oleari and E. Re, *A general framework for implementing NLO calculations in shower Monte Carlo programs: the POWHEG BOX*, JHEP **06** (2010) 043, arXiv: 1002.2581 [hep-ph] (cit. on p. 4).

[46] T. Melia, P. Nason, R. Rontsch and G. Zanderighi,
W^+W^-, WZ and ZZ production in the POWHEG BOX, JHEP **11** (2011) 078,
arXiv: 1107.5051 [hep-ph] (cit. on p. 4).

[47] P. Nason and G. Zanderighi, *W^+W^-, WZ and ZZ production in the POWHEG-BOX-V2*,
Eur. Phys. J. C **74** (2014) 2702, arXiv: 1311.1365 [hep-ph] (cit. on p. 4).

[48] T. Sjöstrand, S. Mrenna and P. Skands, *A brief introduction to PYTHIA 8.1*,
Comput. Phys. Commun. **178** (2008) 852, arXiv: 0710.3820 [hep-ph] (cit. on p. 4).

[49] ATLAS Collaboration, *Measurement of the Z/γ^* boson transverse momentum distribution in pp collisions at $\sqrt{s} = 7$ TeV with the ATLAS detector*, JHEP **09** (2014) 145,
arXiv: 1406.3660 [hep-ex] (cit. on p. 4).

[50] H.-L. Lai et al., *New parton distributions for collider physics*, Phys. Rev. D **82** (2010) 074024,
arXiv: 1007.2241 [hep-ph] (cit. on p. 4).

[51] J. Pumplin et al.,
New Generation of Parton Distributions with Uncertainties from Global QCD Analysis,
JHEP **07** (2002) 012, arXiv: hep-ph/0201195 (cit. on p. 4).

[52] F. Cascioli et al., *ZZ production at hadron colliders in NNLO QCD*, Phys. Lett. B **735** (2014) 311,
arXiv: 1405.2219 [hep-ph] (cit. on p. 4).

[53] M. Grazzini, S. Kallweit and D. Rathlev,
ZZ production at the LHC: fiducial cross sections and distributions in NNLO QCD,
Phys. Lett. B **750** (2015) 407, arXiv: 1507.06257 [hep-ph] (cit. on p. 4).

[54] M. Grazzini, S. Kallweit and M. Wiesemann, *Fully differential NNLO computations with MATRIX*,
Eur. Phys. J. C **78** (2018) 537, arXiv: 1711.06631 [hep-ph] (cit. on p. 4).

[55] S. Kallweit and M. Wiesemann,
ZZ production at the LHC: NNLO predictions for $2\ell 2\nu$ and 4ℓ signatures,
Phys. Lett. B **786** (2018) 382, arXiv: 1806.05941 [hep-ph] (cit. on p. 4).

[56] ATLAS Collaboration, *Measurements of differential cross-sections in four-lepton events in 13 TeV proton–proton collisions with the ATLAS detector*, JHEP **07** (2021) 005,
arXiv: 2103.01918 [hep-ex] (cit. on p. 4).

[57] F. Caola, K. Melnikov, R. Röntsch and L. Tancredi,
QCD corrections to ZZ production in gluon fusion at the LHC, Phys. Rev. D **92** (2015) 094028,
arXiv: 1509.06734 [hep-ph] (cit. on p. 4).

[58] F. Caola, M. Dowling, K. Melnikov, R. Röntsch and L. Tancredi, *QCD corrections to vector boson pair production in gluon fusion including interference effects with off-shell Higgs at the LHC*,
JHEP **07** (2016) 087, arXiv: 1605.04610 [hep-ph] (cit. on pp. 4, 14).

[59] G. Passarino, *Higgs CAT*, Eur. Phys. J. C **74** (2014) 2866, arXiv: 1312.2397 [hep-ph]
(cit. on p. 4).

[60] D. de Florian et al.,
Handbook of LHC Higgs Cross Sections: 4. Deciphering the Nature of the Higgs Sector, (2016),
arXiv: 1610.07922 [hep-ph] (cit. on p. 4).

[61] J. Alwall et al., *The automated computation of tree-level and next-to-leading order differential cross sections, and their matching to parton shower simulations*, JHEP **07** (2014) 079,
arXiv: 1405.0301 [hep-ph] (cit. on p. 4).

[62] T. Sjöstrand et al., *An introduction to PYTHIA 8.2*, Comput. Phys. Commun. **191** (2015) 159, arXiv: 1410.3012 [hep-ph] (cit. on p. 4).

[63] ATLAS Collaboration, *ATLAS Pythia 8 tunes to 7 TeV data*, ATL-PHYS-PUB-2014-021, 2014, URL: https://cds.cern.ch/record/1966419 (cit. on p. 4).

[64] D. Buarque Franzosi, O. Mattelaer, R. Ruiz and S. Shil, *Automated predictions from polarized matrix elements*, JHEP **04** (2020) 082, arXiv: 1912.01725 [hep-ph] (cit. on p. 4).

[65] NNPDF Collaboration, R. D. Ball et al., *Parton distributions with LHC data*, Nucl. Phys. B **867** (2013) 244, arXiv: 1207.1303 [hep-ph] (cit. on p. 4).

[66] A. Denner and G. Pelliccioli, *NLO EW and QCD corrections to polarized ZZ production in the four-charged-lepton channel at the LHC*, JHEP **10** (2021) 097, arXiv: 2107.06579 [hep-ph] (cit. on pp. 5, 9, 10, 14).

[67] L. Lönnblad, *Correcting the Colour-Dipole Cascade Model with Fixed Order Matrix Elements*, JHEP **05** (2002) 046, arXiv: hep-ph/0112284 (cit. on p. 5).

[68] L. Lönnblad and S. Prestel, *Matching tree-level matrix elements with interleaved showers*, JHEP **03** (2012) 019, arXiv: 1109.4829 [hep-ph] (cit. on p. 5).

[69] ATLAS Collaboration, *Measurement of the $t\bar{t}Z$ and $t\bar{t}W$ cross sections in proton–proton collisions at $\sqrt{s}$ = 13 TeV with the ATLAS detector*, Phys. Rev. D **99** (2019) 072009, arXiv: 1901.03584 [hep-ex] (cit. on p. 5).

[70] ATLAS Collaboration, *Evidence for the production of three massive vector bosons with the ATLAS detector*, Phys. Lett. B **798** (2019) 134913, arXiv: 1903.10415 [hep-ex] (cit. on p. 5).

[71] C. Anastasiou, L. Dixon, K. Melnikov and F. Petriello, *High-precision QCD at hadron colliders: Electroweak gauge boson rapidity distributions at next-to-next-to leading order*, Phys. Rev. D **69** (2004) 094008, arXiv: hep-ph/0312266 (cit. on p. 5).

[72] C. Degrande et al., *UFO - The Universal FeynRules Output*, Comput. Phys. Commun. **183** (2012) 1201, arXiv: 1108.2040 [hep-ph] (cit. on p. 5).

[73] ATLAS Collaboration, *The ATLAS Simulation Infrastructure*, Eur. Phys. J. C **70** (2010) 823, arXiv: 1005.4568 [physics.ins-det] (cit. on p. 5).

[74] S. Agostinelli et al., *GEANT4 – a simulation toolkit*, Nucl. Instrum. Meth. A **506** (2003) 250 (cit. on p. 5).

[75] ATLAS Collaboration, *The Pythia 8 A3 tune description of ATLAS minimum bias and inelastic measurements incorporating the Donnachie–Landshoff diffractive model*, ATL-PHYS-PUB-2016-017, 2016, URL: https://cds.cern.ch/record/2206965 (cit. on p. 5).

[76] ATLAS Collaboration, *Electron reconstruction and identification in the ATLAS experiment using the 2015 and 2016 LHC proton–proton collision data at $\sqrt{s}$ = 13 TeV*, Eur. Phys. J. C **79** (2019) 639, arXiv: 1902.04655 [hep-ex] (cit. on pp. 6, 14).

[77] ATLAS Collaboration, *Electron and photon performance measurements with the ATLAS detector using the 2015–2017 LHC proton–proton collision data*, JINST **14** (2019) P12006, arXiv: 1908.00005 [hep-ex] (cit. on pp. 6, 7).

[78] ATLAS Collaboration, *Muon reconstruction and identification efficiency in ATLAS using the full Run 2 pp collision data set at* $\sqrt{s}$ = 13 *TeV*, Eur. Phys. J. C **81** (2021) 578, arXiv: 2012.00578 [hep-ex] (cit. on pp. 7, 14).

[79] ATLAS Collaboration, *Muon reconstruction performance of the ATLAS detector in proton–proton collision data at* $\sqrt{s}$ = 13 *TeV*, Eur. Phys. J. C **76** (2016) 292, arXiv: 1603.05598 [hep-ex] (cit. on p. 7).

[80] M. Cacciari, G. P. Salam and G. Soyez, *The anti-k_t jet clustering algorithm*, JHEP **04** (2008) 063, arXiv: 0802.1189 [hep-ph] (cit. on p. 7).

[81] ATLAS Collaboration, *Jet reconstruction and performance using particle flow with the ATLAS Detector*, Eur. Phys. J. C **77** (2017) 466, arXiv: 1703.10485 [hep-ex] (cit. on p. 7).

[82] ATLAS Collaboration, *ATLAS b-jet identification performance and efficiency measurement with $t\bar{t}$ events in pp collisions at* $\sqrt{s}$ = 13 *TeV*, Eur. Phys. J. C **79** (2019) 970, arXiv: 1907.05120 [hep-ex] (cit. on p. 7).

[83] ATLAS Collaboration, *ATLAS flavour-tagging algorithms for the LHC Run 2 pp collision dataset*, (2022), arXiv: 2211.16345 [physics.data-an] (cit. on p. 7).

[84] W. J. Stirling and E. Vryonidou, *Electroweak gauge boson polarisation at the LHC*, JHEP **07** (2012) 124, arXiv: 1204.6427 [hep-ph] (cit. on p. 9).

[85] A. Hoecker et al., *TMVA - Toolkit for Multivariate Data Analysis*, 2007, arXiv: physics/0703039 [physics.data-an] (cit. on p. 9).

[86] L. Moneta et al., *The RooStats Project*, PoS **ACAT2010** (2010) 057, arXiv: 1009.1003 [physics.data-an] (cit. on p. 10).

[87] W. Verkerke and D. Kirkby, *The RooFit toolkit for data modeling*, 2003, arXiv: physics/0306116 [physics.data-an] (cit. on p. 10).

[88] K. Cranmer, G. Lewis, L. Moneta, A. Shibata and W. Verkerke, *HistFactory: A tool for creating statistical models for use with RooFit and RooStats*, tech. rep., New York U., 2012, URL: https://cds.cern.ch/record/1456844 (cit. on p. 10).

[89] F. Boudjema and R. K. Singh, *A Model independent spin analysis of fundamental particles using azimuthal asymmetries*, JHEP **07** (2009) 028, arXiv: 0903.4705 [hep-ph] (cit. on p. 11).

[90] G. D'Agostini, *A multidimensional unfolding method based on Bayes' theorem*, Nucl. Instrum. Meth. A **362** (1995) 487 (cit. on p. 13).

[91] J. Butterworth et al., *PDF4LHC recommendations for LHC Run II*, J. Phys. G **43** (2016) 023001, arXiv: 1510.03865 [hep-ph] (cit. on p. 14).

[92] L. A. Harland-Lang, A. D. Martin, P. Motylinski and R. S. Thorne, *Parton distributions in the LHC era: MMHT 2014 PDFs*, Eur. Phys. J. C **75** (2015) 204, arXiv: 1412.3989 [hep-ph] (cit. on p. 14).

[93] S. Dulat et al., *New parton distribution functions from a global analysis of quantum chromodynamics*, Phys. Rev. D **93** (2016) 033006, arXiv: 1506.07443 [hep-ph] (cit. on p. 14).

[94] J. Bellm et al., *Herwig 7.0/Herwig++ 3.0 release note*, Eur. Phys. J. C **76** (2016) 196, arXiv: 1512.01178 [hep-ph] (cit. on p. 14).

[95] M. Bähr et al., *Herwig++ physics and manual*, Eur. Phys. J. C **58** (2008) 639, arXiv: 0803.0883 [hep-ph] (cit. on p. 14).

[96] T. K. S. Gieseke and J. H. Kühn, *Vector-boson pair production and electroweak corrections in HERWIG++*, 2014, arXiv: 1401.3964 [hep-ph] (cit. on p. 14).

[97] ATLAS Collaboration, *Luminosity determination in pp collisions at $\sqrt{s} = 13$ TeV using the ATLAS detector at the LHC*, (2022), arXiv: 2212.09379 [hep-ex] (cit. on p. 14).

[98] ATLAS Collaboration, *Measurement of the Inelastic Proton–Proton Cross Section at $\sqrt{s} = 13$ TeV with the ATLAS Detector at the LHC*, Phys. Rev. Lett. **117** (2016) 182002, arXiv: 1606.02625 [hep-ex] (cit. on p. 14).

[99] G. Cowan, K. Cranmer, E. Gross and O. Vitells, *Asymptotic formulae for likelihood-based tests of new physics*, Eur. Phys. J. C **71** (2011) 1554, arXiv: 1007.1727 [physics.data-an] (cit. on pp. 15, 18), Erratum: Eur. Phys. J. C **73** (2013) 2501.

[100] S. S. Wilks, *The Large-Sample Distribution of the Likelihood Ratio for Testing Composite Hypotheses*, Annals Math. Statist. **9** (1938) 60 (cit. on p. 18).